

# Identification of the 3D crystallographic orientation using 2D deformations

*J Strain Analysis*

1–14

© IMechE 2021

Article reuse guidelines:

sagepub.com/journals-permissions

DOI: 10.1177/03093247211043107

journals.sagepub.com/home/sdj



Sevan Goenezen<sup>1</sup>, Maulik C Kotecha and Junuthula N Reddy

## Abstract

Polycrystalline materials consist of grains (crystals) oriented at different angles resulting in a heterogeneous and anisotropic mechanical behavior at that micro-length scale. In this study, a novel method is proposed for the first time to determine the 3D crystal orientations of grains in a 2D domain, using solely 2D deformation fields. The grain boundaries are assumed to be unknown and delineated from the reconstructed changes in the crystallographic orientation. Further, the constitutive equations that describe the mechanical behavior of the domain in 2D under plane stress conditions are derived, assuming that the material is transversely isotropic in 3D. Finite element based algorithms are utilized to discretize the inverse problem. The in-house written inverse problem solver is coupled with Matlab-based optimization scripts to solve for the mechanical property distributions. The performance of this method is tested at different noise levels with synthetic displacements that were used as measured data. The reconstructions deteriorate as the noise level is increased. This work presents a first milestone in the verification of this novel technology with synthetic data.

## Keywords

Inverse problems, anisotropic elasticity, crystallographic orientation, grain boundaries, grain orientation imaging

Date received: 17 December 2020; accepted: 22 July 2021

## Introduction

In recent years, additive manufacturing technology has tremendously advanced, and its commercial use is growing broadly. This non-conventional manufacturing technique may provide new opportunities to create metal and alloy based materials with tailored spatial variations in their mechanical properties at the macro length scale by altering the grain structure at the micro length scale. This can be achieved through the adjustment of process parameters in additive manufacturing. For example, the elevated power of the laser system (1000 W) increases cooling time, thus produces elongated grains, leading to an anisotropic mechanical response, which could potentially be spatially controlled.<sup>1</sup> Several other factors could potentially cause inhomogeneities in the mechanical properties of additively manufactured parts such as dwell times at elevated temperatures, deposition rate, build environment, directional cooling patterns, etc. to name a few.<sup>2</sup> However, it is highly challenging to adjust process parameters to yield controlled and desired mechanical property distributions. To thoroughly study the effect of process parameters on the mechanical behavior of

the material, it is essential to accurately determine the spatial distribution of the crystal orientations.

Hovig et al.<sup>3</sup> determined the anisotropic elastic properties of Inconel 718 at the macroscopic length scale after additively manufacturing the part using laser powder bed fusion. To this end, tensile tests were conducted at multiple orientations of the build part and the deformation field was measured using a digital image correlation (DIC) system. An optimization method was utilized to infer the linear elastic anisotropic constants. Their method is applicable to homogeneous specimens, and does not reveal spatial variations in the anisotropic properties. Nano-indentations have been employed to measure the elastic properties of anisotropic materials,

Department of Mechanical Engineering, Texas A&M University, College Station, TX, USA  
Engineering Solutions and Quality Products, LLC, San Marcos, TX 78666, USA

## Corresponding author:

Sevan Goenezen, Department of Mechanical Engineering, Texas A&M University, J. Mike Walker 66', 3123 Spence Street, College Station, TX 77840, USA

Email: sevangoeenen@gmail.com

including cubic and transversely isotropic single crystals.<sup>4</sup> These methods are locally applied and do not accommodate a continuous quantification of the mechanical property distribution.

Herrera-Solaz et al.<sup>5</sup> described an iterative optimization strategy based on the Levenberg–Marquardt method to determine the single-crystal mechanical behavior of magnesium alloy (AZ31). They used multi-scale modeling with finite element methods and incorporated multiple simulated tests in their optimization process. Pant et al.<sup>6</sup> demonstrated a methodology based on ultrasonic wave velocities to characterize homogeneous elastic properties of transversely isotropic materials. The approaches in Herrera-Solaz et al.<sup>5</sup> and Pant et al.<sup>6</sup> require homogeneity of the specimen and thus limit their applicability to analyze process parameters in additive manufacturing.

In previous works, the corresponding author of this paper has demonstrated feasibility to recover the orthotropic elastic property distribution in 2D utilizing in plane displacement fields.<sup>7</sup> In this paper, we propose a novel approach to determine the three dimensional (3D) angular orientation distribution of a polycrystalline material at the micro length scale by utilizing solely two dimensional (2D) displacement fields in plane. We conduct a theoretical study using a thin plate like sample at the grain length scale with multiple grains and create synthetic displacement fields in 2D to test feasibility of our approach. These synthetic displacement fields are augmented with various noise levels to mimic noise in measurements. An in-house written optimization program is utilized to solve the inverse problem, which is posed as a constrained minimization problem. This theoretical framework represents the first step of a potentially new technology to map the crystal orientation in 3D and grain boundaries solely from 2D displacement measurements.

## Method

In this section, we derive the constitutive equations to describe the plane stress response of a three dimensional (3D) transversely isotropic material. This strategy results in two dimensional (2D) boundary value problems that preserve the 3D directional dependency of the crystallographic orientation in a plane. We assume a linear elastic material behavior and start with the generalized Hooke's law given in the following form:

$$\epsilon_{ij}^{xyz} = S_{ijkl}^{xyz} \sigma_{kl}^{xyz} \quad (1)$$

Here,  $S_{ijkl}^{xyz}$  are the fourth order elastic compliance tensor components, and  $\epsilon_{ij}^{xyz}$  and  $\sigma_{kl}^{xyz}$  are strain and stress tensors, respectively. The superscript with lowercase letters "xyz" denotes the variables with respect to the local coordinate system aligned with the material orientation.

Adopting Voigt notation the 3D stress and strain tensors can be written in the following form:

$$\begin{aligned} \sigma_{voigt}^{xyz} &= \begin{pmatrix} \sigma_1^{xyz} \\ \sigma_2^{xyz} \\ \sigma_3^{xyz} \\ \sigma_4^{xyz} \\ \sigma_5^{xyz} \\ \sigma_6^{xyz} \end{pmatrix} = \begin{pmatrix} \sigma_{11}^{xyz} \\ \sigma_{22}^{xyz} \\ \sigma_{33}^{xyz} \\ \sigma_{23}^{xyz} \\ \sigma_{31}^{xyz} \\ \sigma_{12}^{xyz} \end{pmatrix}; \\ \epsilon_{voigt}^{xyz} &= \begin{pmatrix} \epsilon_1^{xyz} \\ \epsilon_2^{xyz} \\ \epsilon_3^{xyz} \\ \epsilon_4^{xyz} \\ \epsilon_5^{xyz} \\ \epsilon_6^{xyz} \end{pmatrix} = \begin{pmatrix} \epsilon_{11}^{xyz} \\ \epsilon_{22}^{xyz} \\ \epsilon_{33}^{xyz} \\ \epsilon_{23}^{xyz} \\ \epsilon_{31}^{xyz} \\ \epsilon_{12}^{xyz} \end{pmatrix} \end{aligned} \quad (2)$$

Further, assuming a transversely isotropic material, the fourth order elastic compliance tensor can be represented by a 6×6 matrix given by:

$$\begin{aligned} \mathbf{S}^{xyz} &= \begin{bmatrix} S_{11} & S_{12} & S_{13} & 0 & 0 & 0 \\ S_{12} & S_{11} & S_{13} & 0 & 0 & 0 \\ S_{13} & S_{13} & S_{33} & 0 & 0 & 0 \\ 0 & 0 & 0 & S_{44} & 0 & 0 \\ 0 & 0 & 0 & 0 & S_{44} & 0 \\ 0 & 0 & 0 & 0 & 0 & S_{66} \end{bmatrix} \\ &= \begin{bmatrix} \frac{1}{E_{xx}} & \frac{-\nu_{xy}}{E_{xx}} & \frac{-\nu_{zx}}{E_{zz}} & 0 & 0 & 0 \\ \frac{-\nu_{xy}}{E_{xx}} & \frac{1}{E_{xx}} & \frac{-\nu_{zx}}{E_{zz}} & 0 & 0 & 0 \\ \frac{-\nu_{zx}}{E_{zz}} & \frac{-\nu_{zx}}{E_{zz}} & \frac{1}{E_{zz}} & 0 & 0 & 0 \\ 0 & 0 & 0 & \frac{1}{\mu_{xz}} & 0 & 0 \\ 0 & 0 & 0 & 0 & \frac{1}{\mu_{xz}} & 0 \\ 0 & 0 & 0 & 0 & 0 & \frac{1}{\mu_{xy}} \end{bmatrix} \end{aligned} \quad (3)$$

which contains five independent mechanical parameters  $S_{11}$ ,  $S_{33}$ ,  $S_{44}$ ,  $S_{12}$ , and  $S_{13}$  or more widely used in terms of the elastic constants with physical meaning in engineering,  $E_{xx}$ ,  $E_{zz}$ ,  $\nu_{xy}$ ,  $\nu_{zx}$ , and  $\mu_{xz}$ . Here, it should be noted that  $S_{66} = 2(S_{11} - S_{12})$ . We assume that the orientation of the transversely isotropic material is aligned with the  $z$ -axis, implying that the  $xy$ -plane is isotropic. Further, we note that  $XYZ$  are global coordinates. In the global coordinate frame, we write the generalized Hooke's Law as  $\epsilon^{XYZ} = \mathbf{S}^{XYZ} \sigma^{XYZ}$ , where  $\sigma^{XYZ} = \mathbf{K}^\sigma \sigma^{xyz}$ ,  $\epsilon^{XYZ} = \mathbf{K}^\epsilon \epsilon^{xyz}$ , and  $\mathbf{S}^{XYZ} = \mathbf{K}^\epsilon \mathbf{S}^{xyz} (\mathbf{K}^\sigma)^{-1}$ . The superscript with uppercase letters  $XYZ$  denote the expression with respect to the global coordinate system.

As described in Lekhnitskii et al.<sup>8</sup> and Ting<sup>9</sup> for our chosen convention of representing stress and strain

tensors, it can be shown that  $\mathbf{K}^\sigma = \mathbf{R}$  and  $\mathbf{K}^\epsilon = \mathbf{R}^{-T}$  and thus  $\mathbf{S}^{XYZ} = \mathbf{R}^{-T} \mathbf{S}^{xyz} \mathbf{R}^{-1}$ , where  $\mathbf{R}$  is a  $6 \times 6$  matrix defined in equation (4).

$$\mathbf{R} = \begin{bmatrix} r_{11}^2 & r_{12}^2 & r_{13}^2 & 2r_{12}r_{13} & 2r_{11}r_{13} & 2r_{11}r_{12} \\ r_{21}^2 & r_{22}^2 & r_{23}^2 & 2r_{22}r_{23} & 2r_{23}r_{21} & 2r_{21}r_{22} \\ r_{31}^2 & r_{32}^2 & r_{33}^2 & 2r_{32}r_{33} & 2r_{31}r_{33} & 2r_{31}r_{32} \\ r_{21}r_{31} & r_{22}r_{32} & r_{23}r_{33} & r_{22}r_{33} + r_{23}r_{32} & r_{21}r_{33} + r_{23}r_{31} & r_{21}r_{32} + r_{22}r_{31} \\ r_{31}r_{11} & r_{12}r_{32} & r_{13}r_{33} & r_{12}r_{33} + r_{13}r_{32} & r_{11}r_{33} + r_{13}r_{31} & r_{11}r_{32} + r_{12}r_{31} \\ r_{11}r_{21} & r_{12}r_{22} & r_{13}r_{23} & r_{12}r_{23} + r_{13}r_{22} & r_{11}r_{23} + r_{13}r_{21} & r_{11}r_{22} + r_{12}r_{21} \end{bmatrix} \quad (4)$$

Here,  $r_{ij}$  are the components of the orthogonal rotation matrix given by

$$\mathbf{Q} = \begin{pmatrix} r_{11} & r_{12} & r_{13} \\ r_{21} & r_{22} & r_{23} \\ r_{31} & r_{32} & r_{33} \end{pmatrix} \quad (5)$$

In the following, we define the orthogonal rotation matrix  $\mathbf{Q}$  via three consecutive rotations about the coordinate axis. We perform the rotations starting from the local coordinate system into the global coordi-

$$\mathbf{Q} = \mathbf{Q}_{x''}(\alpha) \mathbf{Q}_{y'}(\beta) \mathbf{Q}_z(\gamma) \quad (6)$$

$$\begin{aligned} \mathbf{Q}_z(\gamma) &= \begin{pmatrix} \cos(\gamma) & \sin(\gamma) & 0 \\ -\sin(\gamma) & \cos(\gamma) & 0 \\ 0 & 0 & 1 \end{pmatrix}; \\ \mathbf{Q}_{y'}(\beta) &= \begin{pmatrix} \cos(\beta) & 0 & -\sin(\beta) \\ 0 & 1 & 0 \\ \sin(\beta) & 0 & \cos(\beta) \end{pmatrix}; \\ \mathbf{Q}_{x''}(\alpha) &= \begin{pmatrix} 1 & 0 & 0 \\ 0 & \cos(\alpha) & \sin(\alpha) \\ 0 & -\sin(\alpha) & \cos(\alpha) \end{pmatrix} \end{aligned}$$

$$\begin{aligned} \mathbf{Q} &= \begin{pmatrix} r_{11} & r_{12} & r_{13} \\ r_{21} & r_{22} & r_{23} \\ r_{31} & r_{32} & r_{33} \end{pmatrix} \\ &= \begin{pmatrix} \cos(\beta) \cos(\gamma) & \cos(\beta) \sin(\gamma) & -\sin(\beta) \\ \cos(\gamma) \sin(\alpha) \sin(\beta) - \cos(\alpha) \sin(\gamma) & \cos(\alpha) \cos(\gamma) + \sin(\alpha) \sin(\beta) \sin(\gamma) & \cos(\beta) \sin(\alpha) \\ \sin(\alpha) \sin(\gamma) + \cos(\alpha) \cos(\gamma) \sin(\beta) & \cos(\alpha) \sin(\beta) \sin(\gamma) - \cos(\gamma) \sin(\alpha) & \cos(\alpha) \cos(\beta) \end{pmatrix} \end{aligned} \quad (7)$$

nate system as shown in Figure 1. We perform rotations of material coordinates in the order  $z - y' - x''$  by Euler angles  $\gamma, \beta$ , and  $\alpha$  (Figure 2, equation (6)). There are several other combinations for the order in which we can make the rotations to achieve the desired orientation known as *Euler Angles*. We use the order of

The components of  $\mathbf{Q}$  (i.e.  $r_{ij}$ ) are used in the transformation matrix  $\mathbf{R}$  (equation (4)) to obtain the compliance matrix in the global coordinate system ( $\mathbf{S}^{XYZ}$ ). We observe that the terms involving angle  $\gamma$  vanish in the transformed compliance matrix. Physically, this can be explained by the isotropy in the  $xy$ -plane. Next, we derive the constitutive equations for plane stress conditions for a transversely isotropic material. The constitutive equations for our model in Voigt notations are given by

$$\left. \begin{aligned} S_{11}^{XYZ} \sigma_1^{XYZ} + S_{12}^{XYZ} \sigma_2^{XYZ} + S_{13}^{XYZ} \sigma_3^{XYZ} + S_{14}^{XYZ} \sigma_4^{XYZ} + S_{15}^{XYZ} \sigma_5^{XYZ} + S_{16}^{XYZ} \sigma_6^{XYZ} &= \epsilon_1^{XYZ} \\ S_{21}^{XYZ} \sigma_1^{XYZ} + S_{22}^{XYZ} \sigma_2^{XYZ} + S_{23}^{XYZ} \sigma_3^{XYZ} + S_{24}^{XYZ} \sigma_4^{XYZ} + S_{25}^{XYZ} \sigma_5^{XYZ} + S_{26}^{XYZ} \sigma_6^{XYZ} &= \epsilon_2^{XYZ} \\ S_{31}^{XYZ} \sigma_1^{XYZ} + S_{32}^{XYZ} \sigma_2^{XYZ} + S_{33}^{XYZ} \sigma_3^{XYZ} + S_{34}^{XYZ} \sigma_4^{XYZ} + S_{35}^{XYZ} \sigma_5^{XYZ} + S_{36}^{XYZ} \sigma_6^{XYZ} &= \epsilon_3^{XYZ} \\ S_{41}^{XYZ} \sigma_1^{XYZ} + S_{42}^{XYZ} \sigma_2^{XYZ} + S_{43}^{XYZ} \sigma_3^{XYZ} + S_{44}^{XYZ} \sigma_4^{XYZ} + S_{45}^{XYZ} \sigma_5^{XYZ} + S_{46}^{XYZ} \sigma_6^{XYZ} &= \epsilon_4^{XYZ} \\ S_{51}^{XYZ} \sigma_1^{XYZ} + S_{52}^{XYZ} \sigma_2^{XYZ} + S_{53}^{XYZ} \sigma_3^{XYZ} + S_{54}^{XYZ} \sigma_4^{XYZ} + S_{55}^{XYZ} \sigma_5^{XYZ} + S_{56}^{XYZ} \sigma_6^{XYZ} &= \epsilon_5^{XYZ} \\ S_{61}^{XYZ} \sigma_1^{XYZ} + S_{62}^{XYZ} \sigma_2^{XYZ} + S_{63}^{XYZ} \sigma_3^{XYZ} + S_{64}^{XYZ} \sigma_4^{XYZ} + S_{65}^{XYZ} \sigma_5^{XYZ} + S_{66}^{XYZ} \sigma_6^{XYZ} &= \epsilon_6^{XYZ} \end{aligned} \right\} \quad (8)$$

rotation  $z - y' - x''$  as we described earlier, which later on helps us in eliminating one of the angles (angle  $\gamma$  in this case) owing to the symmetries of the transversely isotropic material.

According to the plane stress assumption, the out of plane stress components vanish. Thus, substituting  $\sigma_3^{XYZ} = 0$ ,  $\sigma_4^{XYZ} = 0$ , and  $\sigma_5^{XYZ} = 0$ , we can reduce the six equations (equation (8)) to three equations (equation (9)).

$$\left. \begin{aligned} S_{11}^{XYZ} \sigma_1^{XYZ} + S_{12}^{XYZ} \sigma_2^{XYZ} + S_{16}^{XYZ} \sigma_6^{XYZ} &= \epsilon_1^{XYZ} \\ S_{21}^{XYZ} \sigma_1^{XYZ} + S_{22}^{XYZ} \sigma_2^{XYZ} + S_{23}^{XYZ} \sigma_6^{XYZ} &= \epsilon_2^{XYZ} \\ S_{61}^{XYZ} \sigma_1^{XYZ} + S_{62}^{XYZ} \sigma_2^{XYZ} + S_{66}^{XYZ} \sigma_6^{XYZ} &= \epsilon_6^{XYZ} \end{aligned} \right\} \quad (9)$$

$$\left. \begin{aligned} S_{11}^{XYZ} &= S_{11} - 2 S_{11} \sin^2(\beta) + S_{11} \sin^4(\beta) + 2 S_{13} \sin^2(\beta) \\ &\quad - 2 S_{13} \sin^4(\beta) + S_{33} \sin^4(\beta) + S_{44} \sin^2(\beta) - S_{44} \sin^4(\beta) \\ S_{12}^{XYZ} &= \cos^2(\alpha) (S_{12} \cos^2(\beta) + S_{13} \sin^2(\beta)) + \sin^2(\alpha) \sin^2(\beta) (S_{11} \cos^2(\beta) \\ &\quad + S_{13} \sin^2(\beta)) - S_{44} \cos^2(\beta) \sin^2(\alpha) \sin^2(\beta) \\ &\quad + \cos^2(\beta) \sin^2(\alpha) (S_{13} - S_{13} \sin^2(\beta) + S_{33} \sin^2(\beta)) \\ S_{16}^{XYZ} &= \frac{1}{4} (\sin(\alpha) (2 S_{11} \sin(2\beta) + S_{11} \sin(4\beta) - 2 S_{13} \sin(4\beta) \\ &\quad - 2 S_{33} \sin(2\beta) + S_{33} \sin(4\beta) - S_{44} \sin(4\beta))) \\ S_{22}^{XYZ} &= S_{11} - 2 S_{11} \sin^2(\alpha) + S_{11} \sin^4(\alpha) + 2 S_{13} \sin^2(\alpha) \\ &\quad - 2 S_{13} \sin^4(\alpha) + S_{33} \sin^4(\alpha) + S_{44} \sin^2(\alpha) - S_{44} \sin^4(\alpha) \\ &\quad + 2 S_{11} \sin^2(\alpha) \sin^2(\beta) - 2 S_{11} \sin^4(\alpha) \sin^2(\beta) - 2 S_{13} \sin^2(\alpha) \sin^2(\beta) \\ &\quad + S_{11} \sin^4(\alpha) \sin^4(\beta) + 4 S_{13} \sin^4(\alpha) \sin^2(\beta) - 2 S_{13} \sin^4(\alpha) \sin^4(\beta) \\ &\quad - 2 S_{33} \sin^4(\alpha) \sin^2(\beta) + S_{33} \sin^4(\alpha) \sin^4(\beta) \\ &\quad - S_{44} \sin^2(\alpha) \sin^2(\beta) + 2 S_{44} \sin^4(\alpha) \sin^2(\beta) - S_{44} \sin^4(\alpha) \sin^4(\beta) \\ S_{26}^{XYZ} &= \frac{1}{8} (S_{11} \sin(3\alpha) \sin(2\beta)) + \frac{1}{16} (S_{11} \sin(3\alpha) \sin(4\beta)) \\ &\quad - \frac{1}{4} (S_{13} \sin(3\alpha) \sin(2\beta)) - \frac{1}{8} (S_{13} \sin(3\alpha) \sin(4\beta)) + \frac{1}{8} (S_{33} \sin(3\alpha) \sin(2\beta)) \\ &\quad + \frac{1}{16} (S_{33} \sin(3\alpha) \sin(4\beta)) - \frac{1}{8} (S_{44} \sin(3\alpha) \sin(2\beta)) - \frac{1}{16} (S_{44} \sin(3\alpha) \sin(4\beta)) \\ &\quad + \frac{1}{8} (5 S_{11} \sin(2\beta) \sin(\alpha)) - \frac{1}{16} (3 S_{11} \sin(4\beta) \sin(\alpha)) - \frac{1}{4} (S_{13} \sin(2\beta) \sin(\alpha)) \\ &\quad + \frac{1}{8} (3 S_{13} \sin(4\beta) \sin(\alpha)) - \frac{1}{8} (3 S_{33} \sin(2\beta) \sin(\alpha)) - \frac{1}{16} (3 S_{33} \sin(4\beta) \sin(\alpha)) \\ &\quad - \frac{1}{8} (S_{44} \sin(2\beta) \sin(\alpha)) + \frac{1}{16} (3 S_{44} \sin(4\beta) \sin(\alpha)); \\ S_{66}^{XYZ} &= 2 S_{11} - 2 S_{12} - 2 S_{11} \sin^2(\alpha) + 2 S_{12} \sin^2(\alpha) \\ &\quad + S_{44} \sin^2(\alpha) - 2 S_{11} \sin^2(\beta) + 2 S_{12} \sin^2(\beta) + S_{44} \sin^2(\beta) \\ &\quad + 6 S_{11} \sin^2(\alpha) \sin^2(\beta) - 2 S_{12} \sin^2(\alpha) \sin^2(\beta) - 4 S_{11} \sin^2(\alpha) \sin^4(\beta) \\ &\quad - 8 S_{13} \sin^2(\alpha) \sin^2(\beta) + 8 S_{13} \sin^2(\alpha) \sin^4(\beta) \\ &\quad + 4 S_{33} \sin^2(\alpha) \sin^2(\beta) - 4 S_{33} \sin^2(\alpha) \sin^4(\beta) \\ &\quad - 5 S_{44} \sin^2(\alpha) \sin^2(\beta) + 4 S_{44} \sin^2(\alpha) \sin^4(\beta) \end{aligned} \right\} \quad (10)$$

### Synthetic data generation

We generate synthetic test data for a hypothetical test domain in the  $XY$ -plane (global coordinates) by solving boundary value problems given by:

$$\text{div}(\boldsymbol{\sigma}) = \mathbf{0} \quad \text{on } \Omega \quad (11)$$

$$\mathbf{u} = \mathbf{u}_0 \quad \text{on } \Gamma_u \quad (12)$$

$$\mathbf{t} = \mathbf{t}_0 \quad \text{on } \Gamma_t \quad (13)$$

where,  $\mathbf{u}_0$  represent prescribed displacements on the displacement boundary  $\Gamma_u$  and  $\mathbf{t}_0$  prescribed tractions on the boundary  $\Gamma_t$ . The stress tensor  $\boldsymbol{\sigma}$  can be expressed in terms of the strains using equation (9). We have derived the weak form, discretized it with Galerkin's method, and implemented the algorithms in an in-

house finite element solver. In Figures 3 and 4, we define a heterogeneous domain with side lengths of  $1 \text{ mm} \times 1 \text{ mm}$  and consisting of 16 sub-domains representing individual grains of a hypothetical polycrystal material. To represent the approximate shapes of the grains or crystals in the microstructure of the metal, we used *Voronoi* tessellations. The concept of *Voronoi* diagrams dates back to 17<sup>th</sup> century, when René Descartes, in his book "*Principles of Philosophy*," describing the space decomposed into convex regions and entities of the solar system as its vertices.<sup>10</sup> The concept of crystal-growth has been used to generation of *Voronoi* diagrams and found its applications in various fields.<sup>11</sup> The *Voronoi* diagram represents the grains by randomly created convex polygons. We can generate the *Voronoi* diagrams using randomly located *Voronoi* sites (points). We use the MATLAB command named "*voronoin*" to create the *Voronoi* diagram and a user-

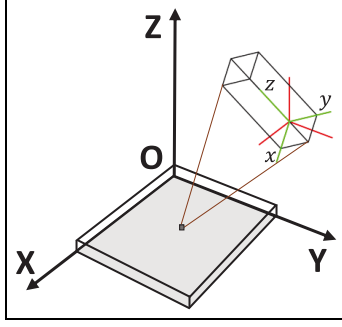


**Figure 1.** Local coordinates for one of the grains that we denote with  $xyz$  alongside the global coordinates ( $XYZ$ ) is also shown.

written MATLAB function called “VoronoiLimit”<sup>12</sup> to confine the Voronoi diagram within the bounds of the problem domain ( $1\text{ mm}^2$  here). We get the vertices of each polygon generated after that and utilize them to assign the nodal properties to the finite element nodes in each of the sub-domain. For our simulations, we limit the average grain sizes to be about  $250\text{ }\mu\text{m}$  in both directions and perturbed the locations of the initially equally spaced Voronoi sites to create the tessellation

of randomly shaped polygons. We used the MATLAB command “convhull” to obtain the closed polygon from the polygon vertices.

We discretize the problem domain in Figure 4 using 20,000 linear triangular finite-elements, and 10,201 finite element nodes. The mesh is uniform and has 101 nodes on each boundary edge. We define a set of six crystallographic orientations via the angles  $\alpha$  and  $\beta$  in Table 1 and assign them to each grain in Table 2. Materials having Hexagonal Closed Packed (HCP) crystal structure such as magnesium, titanium, zinc, etc. are good examples of transversely isotropic materials. The elastic properties of many HCP metals have been reported in the literature.<sup>13</sup> In this study, we use the transversely elastic properties of zinc.<sup>13</sup> Assuming the plane of isotropy being in the  $xy$ -plane, the parameters of the compliance tensor are given by  $S_{11} = 8.07\text{ (T Pa)}^{-1}$ ,  $S_{12} = 0.606\text{ (T Pa)}^{-1}$ ,  $S_{33} = 27.55\text{ (T Pa)}^{-1}$ ,  $S_{44} = 25.25\text{ (T Pa)}^{-1}$ ,  $S_{13} = -7.02\text{ (T Pa)}^{-1}$ . With these parameter values and the angular orientations for each grain, we can calculate the transformed compliance tensor components  $S_{ij}^{XYZ}$  using equation (10). Next, we take the inverse of  $S^{XYZ}$  resulting in the 2D elasticity tensor  $C^{XYZ}$  for each set as shown in Table 3.

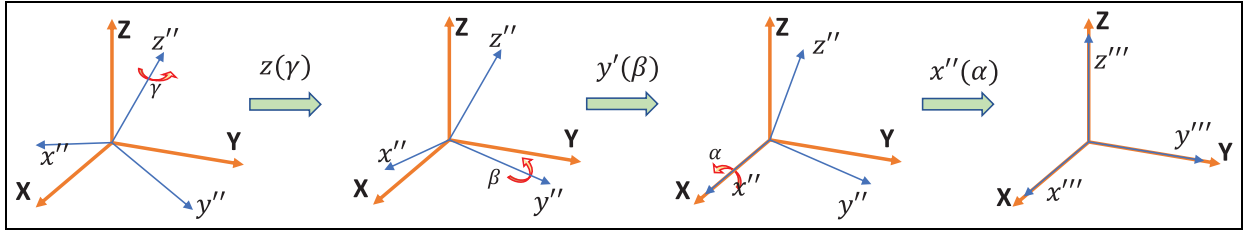


**Figure 2.** Here we illustrate the transformation of the local coordinate system into the global coordinate system.

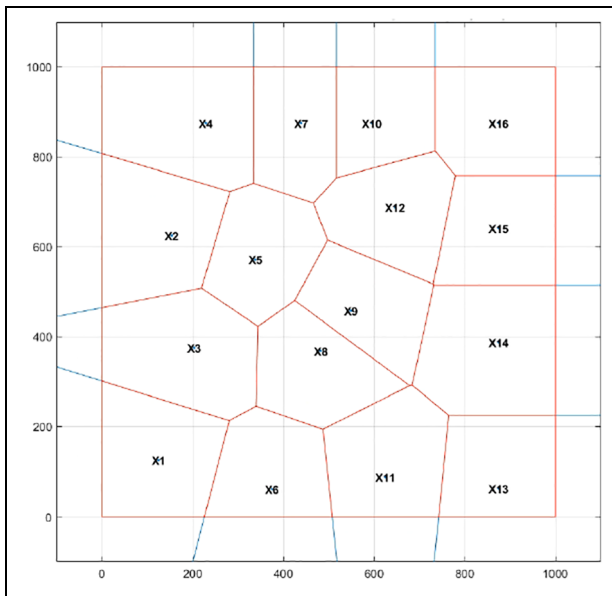


**Figure 3.** Voronoi diagram for a  $1\text{ mm} \times 1\text{ mm}$  bounded square domain with 16 number of Voronoi sites.

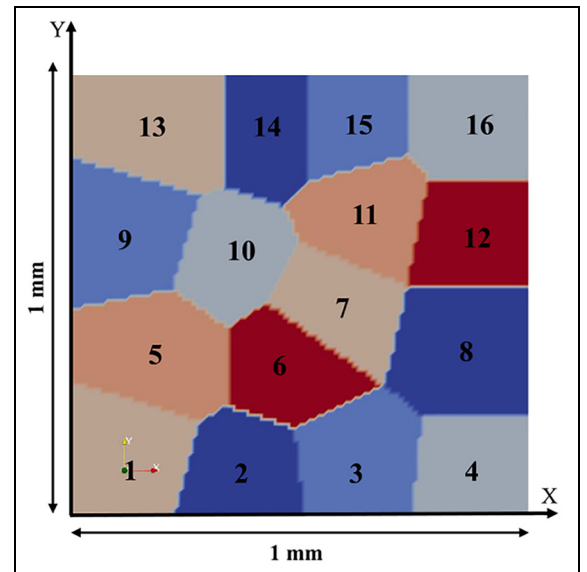


**Figure 4.** Target domain consisting of 16 grains  $1\text{ mm} \times 1\text{ mm}$ .

**Table 1.** Crystallographic angular orientations for each set.

	Set-1	Set-2	Set-3	Set-4	Set-5	Set-6
$\alpha$	$4\pi/9$	$4\pi/9$	$4\pi/9$	$-\pi/10$	$-\pi/30$	$\pi/30$
$\beta$	$\pi/30$	$\pi/4$	$4\pi/9$	$\pi/3$	$\pi/4$	$\pi/36$

**Table 2.** Grain numbers associated with the sets defined in Table 1.

	Set-1	Set-2	Set-3	Set-4	Set-5	Set-6
Grains	6,12	1,7,13	2,8,14	3,9,15	4,10,16	5,11

**Table 3.** Components of the 2D elasticity tensor  $C_{ij}^{XYZ}$  for all sets.

	Set-1	Set-2	Set-3	Set-4	Set-5	Set-6
$C_{11}^{XYZ}$	157.5554	110.9968	50.9468	68.9077	96.0880	124.8967
$C_{12}^{XYZ}$	40.5757	32.1524	39.6201	41.3304	37.8792	-7.2777
$C_{16}^{XYZ}$	3.9721	27.9164	12.1592	-11.0010	-4.3404	-0.3224
$C_{22}^{XYZ}$	50.3008	112.6982	156.8470	150.4821	139.2970	125.1231
$C_{26}^{XYZ}$	7.6066	27.6525	6.8019	-4.0313	-0.2261	-0.3104
$C_{66}^{XYZ}$	39.7004	31.2292	38.6595	42.3534	49.2043	66.1114

### Inverse problem solution

We solve the inverse problem in two steps assuming that the 2D displacement field is available from (synthetic) measurements. First, we solve for six anisotropic elastic parameter distributions  $C_j(\mathbf{x}) = [C_{11}^{XYZ} C_{12}^{XYZ} C_{16}^{XYZ} C_{22}^{XYZ} C_{26}^{XYZ} C_{66}^{XYZ}]$  with  $j = 1, \dots, 6$  that are represented as unknowns on finite element mesh nodes. Thus, this step has a large number of unknowns equal to six times the number of mesh nodes. The solution of this step will reveal each individual grain domain from the contrast in the anisotropic elastic constants. Next, the anisotropic elasticity matrix will be inverted to yield the anisotropic compliance matrix. We have derived the relation of the components of the compliance matrix to the 3D material orientation in equation (10), which is what we are aiming to solve for. We will make use of the recovered grain domains and these equations to solve for these unknowns.

We start with the first step and pose the inverse problem for the unknown anisotropic elastic parameter distributions  $C_j(\mathbf{x})$  as a constrained minimization problem with the boundary value problems (equations (11)–(13)) being the constraints of the problem. The objective function is minimized with respect to the anisotropic elastic constants  $C_j$  and is given by:

$$\pi = \frac{1}{2} \sum_{i=1}^{N_{meas}} \|\mathbf{u}_i^{comp}(C_j(\mathbf{x})) - \mathbf{u}_i^{meas}\|^2 + \sum_{j=1}^6 \frac{\alpha_j}{2} \int_{\Omega_0} \sqrt{|\nabla C_j(\mathbf{x})|^2 + c^2} d\Omega \quad (14)$$

The first term represents the displacement correlation term, where the difference between measured and computed displacement fields is minimized in the  $L^2$  norm. The computed displacement fields satisfy the constraints of the boundary value problems that are solved using finite element methods.<sup>14</sup> We observe a summation from  $i = 1, \dots, N_{meas}$  to accommodate multiple measurements, that is, multiple displacement fields from multiple measurements by utilizing distinct boundary conditions. This is important in order to steer the problem to a unique solution as shown in Luo et al.,<sup>15</sup> Barbone and Gokhale.<sup>16</sup> Further, the second term, represents the regularization term to smooth the overall solution of the ill-posed inverse problem. We use the total variation diminishing regularization to preserve sharp grain boundaries. We note that the summation is over six terms, since we have six anisotropic elastic constants to solve for. The constant  $c = 0.01$  is chosen to be a small value to avoid singularities in gradient calculations. The regularization factor  $\alpha$  provides a weight relative to the displacement correlation term and is chosen according to Morozov's discrepancy principle. We utilize a gradient based optimization method to solve the inverse problem. In particular, we make use of the limited BFGS method with readily available subroutines provided in Zhu et al.<sup>17</sup> The gradient is evaluated efficiently using the adjoint equations detailed in Oberai et al.<sup>18</sup> We have discretized and implemented these algorithms into an in-house written program in parallel using message passing interface (MPI). The linear equations are solved using the direct sparse solver in PARDISO.<sup>19–21</sup>

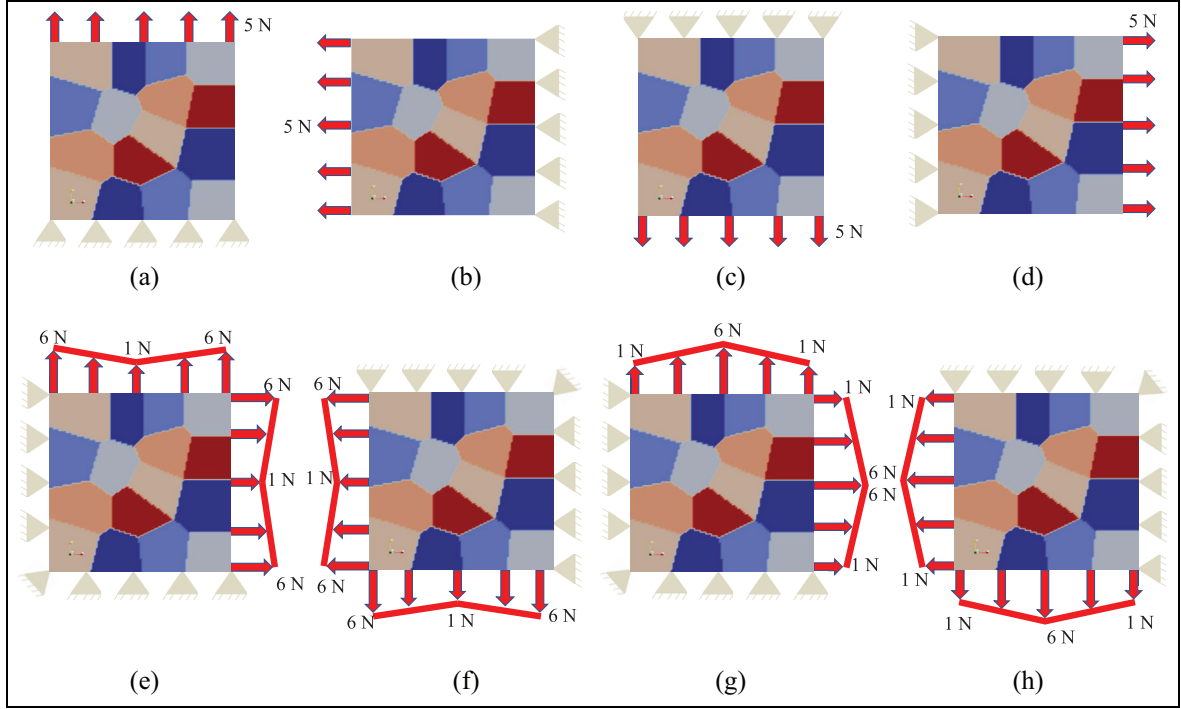


**Figure 5.** Problem domain with grains and varying boundary conditions. Each figure (a-h) has distinctly applied boundary conditions to yield a distinct displacement field.

Next, we delineate the grain boundaries based on the anisotropic elastic parameter contrasts. We then remove outliers within each grain, calculate the compliance matrix at each node (except for the nodes with outliers) by inverting the previously computed anisotropic elasticity matrix. Finally, we take the nodal average values for each component of the compliance matrix ( $(\bar{S}_{ij}^{XYZ})^{(g)}$ ). We use these averaged values within each grain to minimize the following objective functions with respect to the angular orientation within each grain.

$$\begin{aligned}
 eq_{(6(g-1)+1)} &= (S_{11}^{XYZ})^{(g)} - (\bar{S}_{11}^{XYZ})^{(g)} \\
 eq_{(6(g-1)+2)} &= (S_{12}^{XYZ})^{(g)} - (\bar{S}_{12}^{XYZ})^{(g)} \\
 eq_{(6(g-1)+3)} &= (S_{16}^{XYZ})^{(g)} - (\bar{S}_{16}^{XYZ})^{(g)} \\
 eq_{(6(g-1)+4)} &= (S_{22}^{XYZ})^{(g)} - (\bar{S}_{22}^{XYZ})^{(g)} \\
 eq_{(6(g-1)+5)} &= (S_{26}^{XYZ})^{(g)} - (\bar{S}_{26}^{XYZ})^{(g)} \\
 eq_{(6(g-1)+6)} &= (S_{66}^{XYZ})^{(g)} - (\bar{S}_{66}^{XYZ})^{(g)}
 \end{aligned} \tag{15}$$

Here,  $(S_{ij}^{XYZ})^{(g)}$ , for  $g = 1, \dots, G$ , are functions of the mechanical constants  $S_{11}, S_{33}, S_{44}, S_{12}$ , and  $S_{13}$  and the angular orientations  $\alpha^{(g)}$  and  $\beta^{(g)}$  given in equation (10) for each grain and  $G$  is the total number of grains in the problem domain.

We reiterate that we are minimizing equation (15) for two angles at each grain, thus, we are minimizing for  $2 \cdot g$  unknowns, where  $g$  represents the number of grains. We used *lsqnonlin* from the optimization toolbox and selected therein the *trust-region-reflective*

optimization algorithm in MATLAB optimization script to solve for unknowns by minimizing our objective function.

## Results

### Reconstructions by solving an inverse problem

To test the solution strategy outlined in the previous section, we create synthetic displacement fields by solving boundary value problems to represent measured displacement fields. Since experimentally acquired data sets contain measurement errors, we add random Gaussian noise to the simulated displacement fields given in equations (16) and (17).

$$\mathbf{u}^{meas} = \mathbf{u} + \boldsymbol{\eta} \tag{16}$$

$$\% \text{ noise} = \frac{\|\boldsymbol{\eta}\|_{\Omega}^2}{\|\mathbf{u}\|_{\Omega}^2} \times 100\% = \sqrt{\frac{\int_{\Omega} \eta^2 d\Omega}{\int_{\Omega} \mathbf{u}^2 d\Omega}} \times 100\% \tag{17}$$

where  $\boldsymbol{\eta}$  denotes the added noise level. In this paper, we add noise levels of about 0.1% and 1% to the displacement fields. Figure 5 shows the target problem domain with varying boundary conditions, resulting in eight distinct displacement fields that are used in solving the inverse problem.

We note that the misfit of computed and measured displacements (first term in equation (14)) of zero is



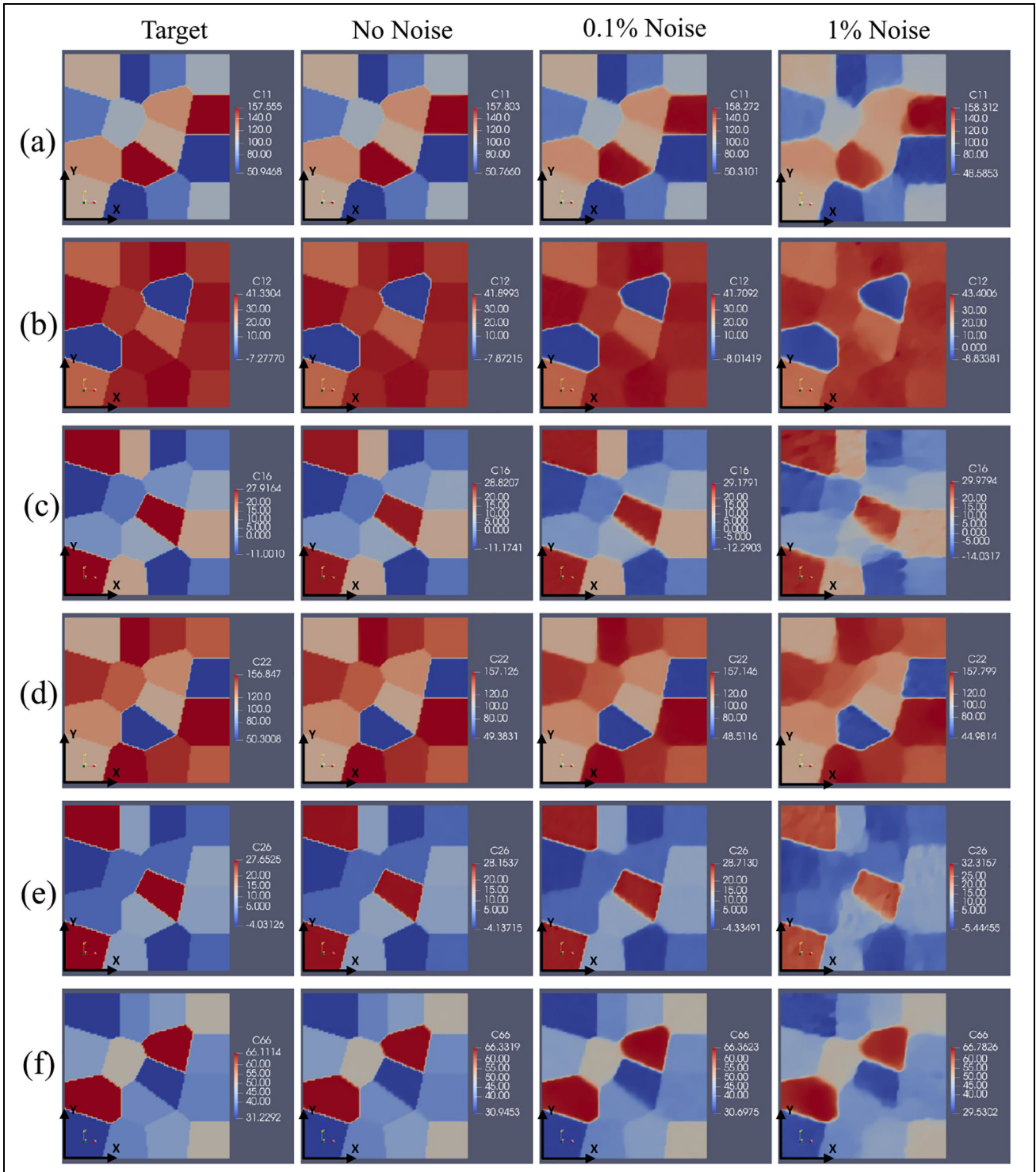


**Figure 6.** Target domain and reconstructions of six parameters using eight synthetic displacement fields: the rows (a–f) depict the target and reconstructed parameter distributions for  $C_{11}^{XYZ}$ ,  $C_{12}^{XYZ}$ ,  $C_{16}^{XYZ}$ ,  $C_{22}^{XYZ}$ ,  $C_{26}^{XYZ}$ , and  $C_{66}^{XYZ}$ , respectively. The first column depicts the target parameter distributions, the second depicts reconstructions without added noise, the third and fourth columns depict the reconstructions with 0.1% and 1% noise, respectively.

only desired if the displacement noise is zero, which is not the case with experimental data sets. For non-zero displacement noise, it is not desired to perfectly match the computed (predicted) displacements with noisy displacement measurements. According to Morozov's discrepancy principle, the misfit between the computed

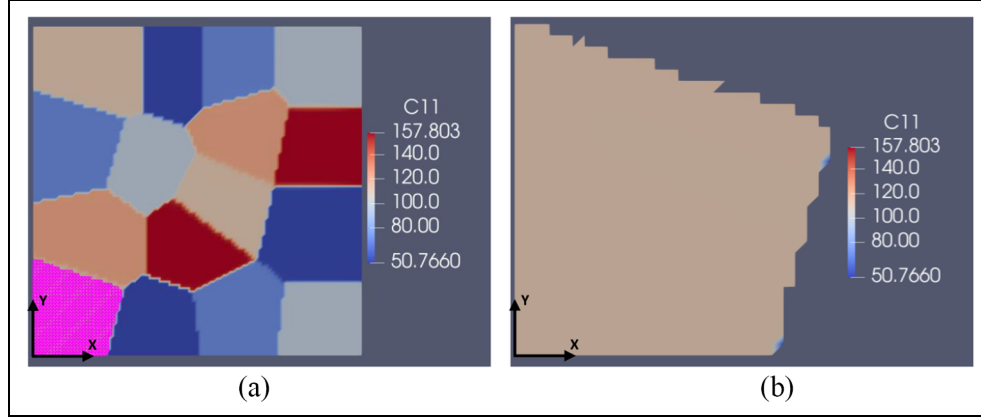
and measured data should be up to the level of noise inherent in the measured data. This misfit in the displacement correlation term is controlled via the regularization term, which can be thought of a penalty term. Setting the regularization factor to zero in the presence of noisy displacement measurements will yield a very



**Table 4.** Regularization parameters, number of iterations, and relative match for different noise levels in the synthetic data.

Noise	$\alpha_1$	$\alpha_2$	$\alpha_3$	$\alpha_4$	$\alpha_5$	$\alpha_6$	Iter.	Rel. match
0%	5.0e-12	5.0e-12	5.0e-12	5.0e-12	5.0e-12	5.0e-12	25,000	0.00076
0.1%	5.0e-10	5.0e-10	5.0e-10	5.0e-10	5.0e-10	5.0e-10	15,807	0.06958
1%	1.0e-8	6.0e-9	8.0e-9	6.0e-9	6.0e-9	6.0e-9	4293	0.69896

Here, the six regularization parameters correspond to the six elastic constants in equation (14).

**Figure 7.** Selecting and extracting individual grains: (a) grain-I with pink mesh overlay, has been selected for further analysis (0% noise) and (b) enlarged view of the extracted domain of grain-I (0% noise).

close fit between computed and measured displacement fields. This would result in reconstructions that are highly oscillatory and far from resembling the target distributions. This reflects the ill-posed nature of the problem and the sensitivity to noise in measured data in the absence of any regularization. As the regularization factor is increased, the misfit in the displacement correlation term increases as well. We have chosen the regularization factor according to Morozov's discrepancy principle. To this end, we have rewritten the displacement correlation term by scaling it with the measured displacement field in the L-2 norm and taking the square root of it as given by

$$\text{relative match} = \sqrt{\frac{\sum_{i=1}^{N_{\text{meas}}} \int_{\Omega} (\mathbf{u}_{\text{comp}}^i(\mathbf{C}(\mathbf{x})) - \mathbf{u}_{\text{meas}}^i(\mathbf{x}))^2 d\Omega}{\sum_{i=1}^{N_{\text{meas}}} \int_{\Omega} (\mathbf{u}_{\text{meas}}^i(\mathbf{x}))^2 d\Omega}} \times 100\% \quad (18)$$

Figure 6 shows the target problem domain in the first panel with all six elastic parameters, followed by the corresponding reconstructions for 0%, 0.1%, and 1% noise in the second, third, and fourth panel, respectively. We observe that the grain domains are very well recovered if no noise is used and start deteriorate as the

noise level increases. We emphasize at this point that these anisotropic elastic property reconstructions in 2D have no direct physical relevance, but serve as an intermediate step in recovering the crystal orientations in each grain. The regularization parameters ( $\alpha_j$ ) pertaining to all six mechanical parameters as well as the number of iterations for the minimization are shown in Table 4 for all three noise levels (i.e. 0%, 0.1%, and 1%). We note that the relative match is in the order of the noise level as shown in our previous publications.<sup>15,22</sup>

### Solving for angular orientations and mechanical parameters for each grain

Next, we delineate grain boundaries from image contrasts in the reconstructions of Figure 6. We illustrate this on a grain sample from Figure 7(a) with a pink overlaid mesh and extracted in Figure 7(b) for the elastic parameter  $C_{11}^{XYZ}$ . We could have selected any other reconstructed elastic parameter as long as the contrast is distinct from its neighboring grains. The fully extracted grain domain is shown in Figure 8 for all noise levels.

After delineating the grain boundaries, we average the elastic parameters within each grain domain after removing outliers. We list the mean reconstructed elasticity parameters (C) in Tables 5 to 7 for 0%, 0.1%, and 1% noise level, respectively.

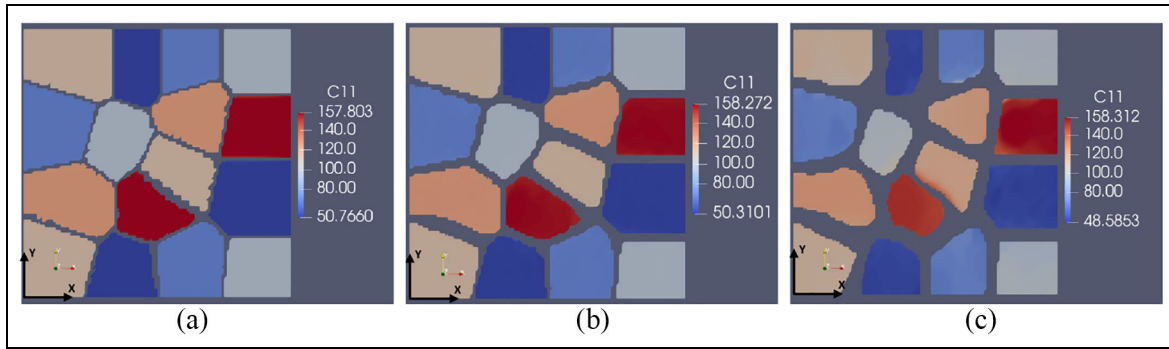


**Figure 8.** Extracted grain domains shown for (a) no noise, (b) 0.1% noise, and (c) 1% noise.

**Table 5.** Mean reconstructed elasticity parameters ( $C$ ) after removing outliers for all 16 grains (0% noise).

Sub-domain	$C_{11}^{XYZ}$	$C_{12}^{XYZ}$	$C_{16}^{XYZ}$	$C_{22}^{XYZ}$	$C_{26}^{XYZ}$	$C_{66}^{XYZ}$
1	111.0116	32.1576	27.9167	112.7035	27.6555	31.2308
2	50.9508	39.6202	12.1574	156.8404	6.7956	38.6578
3	68.9049	41.3331	-11.0076	150.4843	-4.0385	42.3567
4	96.0699	37.8815	-4.3378	139.3150	-0.2241	49.2032
5	124.9008	-7.2806	-0.3264	125.1423	-0.3112	66.1145
6	157.5941	40.5985	3.9446	50.3346	7.5965	39.7236
7	111.0094	32.1542	27.9317	112.7221	27.6620	31.2165
8	50.9322	39.6170	12.1605	156.8406	6.8041	38.6551
9	68.9179	41.3339	-11.0022	150.4801	-4.0338	42.3544
10	96.0911	37.8828	-4.3505	139.3030	-0.2327	49.1990
11	124.8894	-7.2891	-0.3326	125.1161	-0.3036	66.1234
12	157.6092	40.5771	3.9718	50.3038	7.6081	39.6997
13	110.9964	32.1506	27.9184	112.6927	27.6534	31.2278
14	50.9492	39.6217	12.1576	156.8445	6.7948	38.6577
15	68.9339	41.3335	-10.9961	150.5177	-4.0268	42.3521
16	96.0738	37.8853	-4.3397	139.3174	-0.2245	49.2025

**Table 6.** Mean reconstructed elasticity parameters ( $C$ ) after removing outliers for all 16 grains (0.1% noise).

Sub-domain	$C_{11}^{XYZ}$	$C_{12}^{XYZ}$	$C_{16}^{XYZ}$	$C_{22}^{XYZ}$	$C_{26}^{XYZ}$	$C_{66}^{XYZ}$
1	110.9722	32.1612	27.9402	112.7072	27.6757	31.2289
2	50.9238	39.5787	12.1477	156.8037	6.7784	38.6707
3	68.9280	41.3143	-11.0287	150.4987	-4.0257	42.3254
4	96.1134	37.9028	-4.3232	139.3838	-0.2368	49.2162
5	124.9262	-7.3057	-0.3165	125.1628	-0.3129	66.0865
6	157.0173	40.4742	3.9352	50.4789	7.5917	39.7687
7	111.5262	32.3460	27.9368	113.0930	27.5392	31.2275
8	50.8858	39.5901	12.1487	156.7247	6.8345	38.6709
9	68.9198	41.3174	-11.0129	150.3737	-4.0466	42.3452
10	96.2833	37.8713	-4.5023	139.2199	-0.2863	49.1489
11	124.5151	-7.3707	-0.3276	124.9570	-0.3048	66.0244
12	157.5338	40.5774	4.0141	50.3054	7.6127	39.7371
13	110.9353	32.1539	27.9161	112.7245	27.6572	31.2031
14	50.9593	39.6027	12.1402	156.3510	6.7692	38.6605
15	68.8056	41.3255	-11.0027	150.5911	-3.9699	42.3454
16	96.1429	37.8938	-4.3141	139.3664	-0.2197	49.1835

Since we delineated 16 grain domains, the number of unknowns now reduces to  $2 \times 16 = 32$ . Thus, we solve 96 nonlinear equations (6 for each grain) simultaneously to solve for 32 unknowns. We specify the mechanical properties (i.e.  $S_{11}, S_{12}, S_{13}, S_{33}$ , and  $S_{44}$ ),

and solve equations (10) via a nonlinear least-square minimization method using the trust-region-reflective algorithm with the *lsqnonlin* solver from the MATLAB Optimization Toolbox. To analyze uniqueness of the solution, we utilize the multi-start global optimization

**Table 7.** Mean reconstructed elasticity parameters ( $C$ ) after removing outliers for all 16 grains (1% noise).

Sub-domain	$C_{11}^{XYZ}$	$C_{12}^{XYZ}$	$C_{16}^{XYZ}$	$C_{22}^{XYZ}$	$C_{26}^{XYZ}$	$C_{66}^{XYZ}$
1	111.2213	32.2554	27.9552	113.0634	27.7988	31.0537
2	51.3838	39.8460	12.2253	156.7449	7.1354	38.4439
3	69.5607	41.3657	-11.1098	150.4288	-4.1856	42.7308
4	96.1439	37.9999	-4.0697	139.9960	-0.3295	48.9028
5	123.5211	-7.0873	-0.0108	125.1402	-0.5434	65.9398
6	150.3939	39.0876	4.5326	49.9444	7.7571	39.4874
7	119.5652	33.9044	20.9682	105.2789	22.8188	32.7006
8	51.1510	39.8330	11.9250	155.7832	7.0037	38.6946
9	69.1590	41.2927	-11.2992	150.5276	-4.1785	42.3945
10	98.0099	38.5187	-5.3870	139.3666	-0.9246	48.9778
11	120.0847	-7.7697	0.4117	123.9264	-0.1815	64.9721
12	155.8465	40.5771	3.7980	50.4938	7.5086	40.2038
14	111.3397	32.1170	27.8652	112.7025	27.5703	31.1073
15	50.8840	39.4745	12.4693	154.8576	6.7620	38.7972
16	68.7032	41.9779	-11.3043	150.5722	-3.5618	42.7594
17	96.4685	37.8415	-3.8039	139.5396	-0.3974	48.4416

**Table 8.** Optimization options.

Algorithm	“trust-region-reflective”
Display	“iter”
MaxFunctionEvaluations	15,000
OptimalityTolerance	1.00E-14
MaxIterations	15,000
SpecifyObjectiveGradient	0
StepTolerance	1.00E-14
FunctionTolerance	1.00E-25
ConstraintTolerance	1.00E-06
FiniteDifferenceStepSize	“sqrt (eps)”
FiniteDifferenceType	“forward”
SubproblemAlgorithm	“factorization”

**Table 9.** Multi-start global optimization options.

Number of start points	10,001
FunctionTolerance	1.00E-06
MaxTime	30,000
XTolerance	0.1

feature in the Global Optimization Toolbox to solve the minimization problem with multiple starting points. The specified optimization bounds for the angle pairs are  $-\pi/2 \leq \alpha_g \leq \pi/2$ , and  $-\pi/2 \leq \beta_g \leq \pi/2$ . The optimization options are listed in Tables 8 and 9. Table 10 presents the solution for the crystallographic angles for each grain for different noise levels together with their target values.

## Discussions

In this paper, we have presented a new methodology to determine the 3D crystallographic orientations of grains using solely 2D displacement fields. To this end we reduced the 3D constitutive equations to 2D assuming plane stress conditions. The 2D formulation preserves all elastic constants ( $S_{11}$ ,  $S_{12}$ ,  $S_{13}$ ,  $S_{33}$ , and  $S_{44}$ ) and the crystal orientations  $\alpha$  and  $\beta$  from the 3D model. The advantage of the 2D model is that the number of degrees of freedom is significantly reduced and with that the computational time as well. While this work presents a theoretical proof of concept, it is a first step in the verification of this new technology using

synthetic displacements that were augmented with random Gaussian noise levels of 0.1% and 1% to represent noisy measurements. We created synthetic displacements by solving boundary value problems with the finite element method.

Typical measured noise levels with a DIC system for large specimens are in the order of 1% based on our experience with basic experiments on rubber like specimens (Goenezen et al.<sup>23</sup>) with regular camera systems. In the following, we provide a few examples of DIC data acquisition for micro-scale sized region of interests, which are generally imaged with an optical microscope or a scanning electron microscope (SEM). Carroll et al.<sup>24</sup> utilized an optical microscope (Olympus model BX51 M) to measure the strain field of Hastelloy during crack growth with an average grain size of  $95 \mu\text{m}$ . The region of interest was chosen to be  $700 \times 800 \mu\text{m}^2$  with a spatial resolution of  $0.87 \mu\text{m}$  and a pixel size of  $87 \text{nm}$ . EBSD images were provided alongside with a plastic strain distribution in the order of 1%. The authors therein report that about 0.1% strain contributes to the error in the measured strain, which is high given that elastic strains for many metals and alloys are in the order of 0.1%. An SEM DIC system has been used by Di Gioacchino and Quinta da Fonseca<sup>25</sup> to measure plastic strain fields of stainless steel at a spatial resolution of  $0.2 \mu\text{m}$  and a pixel size of  $36 \text{nm}$ . The Sirion FEI SEM system enables the acquisition of high definition images of up to  $4134 \times 2904$  pixels. Fine speckle patterns were achieved by depositing vaporized gold particles. A field of view of

**Table 10.** Reconstructed crystallographic angles for 16 grains.

Angles	Target angles (rad)	0% noise (rad)	0.1% noise (rad)	1% noise (rad)
$\alpha_1$	1.3963	1.3963	1.4006	1.4484
$\beta_1$	0.7854	0.7854	0.7859	0.7885
$\alpha_2$	1.3963	1.3963	1.3893	1.1973
$\beta_2$	1.3963	1.3963	1.3962	1.3828
$\alpha_3$	-0.3142	-0.3142	-0.3156	-0.3051
$\beta_3$	1.0472	1.0472	1.0470	1.0394
$\alpha_4$	-0.1047	-0.1047	-0.1042	-0.1040
$\beta_4$	0.7854	0.7854	0.7852	0.7868
$\alpha_5$	0.1047	0.1047	0.1058	0.1387
$\beta_5$	0.0873	0.0873	0.0878	0.0407
$\alpha_6$	1.3963	1.3963	1.3868	1.4028
$\beta_6$	0.1047	0.1047	0.1044	0.1062
$\alpha_7$	1.3963	1.3963	1.3761	0.9910
$\beta_7$	0.7854	0.7854	0.7845	0.6225
$\alpha_8$	1.3963	1.3963	1.4577	1.1640
$\beta_8$	1.3963	1.3963	1.3983	1.3882
$\alpha_9$	-0.3142	-0.3142	-0.3146	-0.3195
$\beta_9$	1.0472	1.0472	1.0471	1.0452
$\alpha_{10}$	-0.1047	-0.1047	-0.1090	-0.1283
$\beta_{10}$	0.7854	0.7854	0.7845	0.7780
$\alpha_{11}$	0.1047	0.1047	0.1123	0.1719
$\beta_{11}$	0.0873	0.0873	0.0804	0.0177
$\alpha_{12}$	1.3963	1.3963	1.3956	1.3863
$\beta_{12}$	0.1047	0.1047	0.1044	0.0997
$\alpha_{13}$	1.3963	1.3963	1.4025	1.4063
$\beta_{13}$	0.7854	0.7854	0.7861	0.7855
$\alpha_{14}$	1.3963	1.3963	1.3967	1.5708
$\beta_{14}$	1.3963	1.3963	1.3966	1.3968
$\alpha_{15}$	-0.3142	-0.3142	-0.3150	-0.3143
$\beta_{15}$	1.0472	1.0472	1.0484	1.0560
$\alpha_{16}$	-0.1047	-0.1047	-0.1048	-0.1075
$\beta_{16}$	0.7854	0.7854	0.7852	0.7870

$100 \times 100 \mu\text{m}^2$  was recorded in nine subregions and stitched together to obtain a region of interest of  $300 \times 300 \mu\text{m}^2$ . The strain error appears to be about 0.2% and also in the order of elastic strains. However, we note here the small pixel size of  $36 \text{ nm}$  and the potential of achieving higher accuracy as discussed further below. Pinto et al.<sup>26</sup> measured the strain field of a semi-crystalline polymer using an SEM – DIC system. The region of interest was given with  $105.6 \times 158.9 \mu\text{m}^2$  and a spatial resolution of  $2.2 \mu\text{m}$  with a pixel size of  $55 \text{ nm}$ . The absolute strain noise appears to be high as well what appears to be about 0.2%. Walley et al.<sup>27</sup> measured the strain field for a nickel based superalloy with an SEM – DIC system alongside with the underlying grain structure obtained with EBSD. The speckle pattern was produced with electron beam lithography with speckle sizes ranging from  $0.45$  to  $0.7 \mu\text{m}$  and the pixel size was provided with  $150 \text{ nm}$ . The authors therein report the standard deviations in the noise in the displacement and strain measurements to be about 0.03 pixels ( $4.5 \text{ nm}$ ) and 0.07%, respectively. Sutton et al.<sup>28</sup> achieved a displacement accuracy of 0.02 pixels corresponding to  $1 \text{ nm}$  after correcting for the drift and spatial distortions of the SEM – DIC system with a

resolution of  $1024 \times 884$  pixels. Let's assume we would apply a tensile strain of 0.1% on this domain to remain in the elastic regime. This would imply a displacement noise level of roughly 4% for a very small specimen of about  $50 \mu\text{m}$  length. Increasing the specimen length to  $200 \mu\text{m}$ , while keeping the same resolution or stitching together subregions, will reduce the noise level to roughly 1%. This would correspond to the maximum noise level that was utilized in the theoretical study of this paper to map the crystal orientation of grains leveraging a mechanics based approach. Stinville et al.<sup>29</sup> performed SEM – DIC deformation experiments in the elastic region for a nickel based superalloy and present their results alongside with an EBSD image. The average grain size is given by  $26 \mu\text{m}$  and the region of interest has a width of  $85 \mu\text{m}$ . The SEM has a resolution of  $4096 \times 3775$  pixels. Overall tensile strains of 0.29% are applied to the specimen, which is within the elastic range of the material. The authors therein also report that the absolute error in the strain is quite high with 0.15%.

The noise in the displacement field depends on multiple factors, such as the number of pixels and gray values in each facet (also referred to as window or subset). The error in acquired data decreases with the square root of the number of pixels in a facet. Other factors to affect noise in DIC data include the illumination of the sample during image acquisition, speckle pattern distribution, speckle size, speckle pattern contrast, camera set up and calibration, and vibrations affecting the positioning of the cameras and the specimen. This can be addressed by automatizing the entire process (speckle patterning, calibration, illumination within an enclosed system, mechanical testing, data acquisition, etc.) with minimal user input. Under optimal conditions, displacements can be measured up to 0.01 pixel accuracy with a DIC system, thus, the full potential of DIC systems has not yet been exploited.

The experiments discussed above were conducted on specimens with gage dimensions in the order of millimeters, and only a small subregion of that was imaged with SEM. DIC displacement and strain measurements of their work could be translated into smaller sample sizes achieved by other research groups. For example the review paper by Gianola and Eberl<sup>30</sup> reports tensile testing of nano and micro samples utilizing modified atomic force microscope (AFM) systems. In Du et al.<sup>31</sup> the authors fabricated a micro mechanical testing specimen with dimensions of  $9 \times 2.5 \times 2 \mu\text{m}^3$  using focused ion beam (FIB). The tensile testing was conducted without any pre-loading at small displacement increments of  $7 \text{ nm}$  with a maximum accumulated displacement of  $200 \mu\text{m}$ . The load cell measures forces ranging from 0 to  $25 \text{ mN}$  with a precision of  $2.5 \mu\text{N}$ . The reproducible overall strain is reported to be about 0.1% and in the elastic region of many metals and alloys, but no error estimates have been provided. EBSD images are included as well in their work.

Finally, we note that the gage length of specimens can be changed to reduce the overall strain for displacement controlled tensile testing in order to ensure elastic deformations. The region of interest can be a subregion of the test specimen. However, the dimensions of the test specimen may not be too large in particular along the specimen thickness to avoid variations in the grain morphology, since our model assumes plane stress conditions.

This work could help researchers in advanced manufacturing to understand the correlation between various process parameters and their effect on the grain morphology. The grain morphology is also of high interest in Materials Science to predict mechanical properties, surface properties, damage, and annealing behavior that depend on the grain size distribution and orientation.<sup>32,33</sup> Further, magnetic properties, electrical properties, and fracture behavior are affected by their grain orientation and boundaries. Thus, it is of high importance to have the tools to visualize the crystallographic orientation of grains in 3D, which is currently most widely achieved using an electron backscatter diffraction (EBSD). The grain boundaries are then delineated using an image segmentation program that checks for changes in crystallographic orientations.

The proposed method in this paper could potentially provide an alternative to EBSD using the mechanical deformations of materials and mechanics based algorithms to map the crystal orientation. At this developmental stage, however, it is difficult to state if this technology may become a better alternative to EBSD with respect to experimental time, cost, and accuracy of crystallographic orientation maps. We note that the DIC process requires micro sized sample preparation, fine surface polishing, and speckle patterning, for example, using a spray, electron beam lithography, or vaporized gold particles. Furthermore, EBSD appears to be capable of resolving chaotic textures with very fine features. In contrast, the use of Voronoi Tesselation in this paper lead to a well organized grain domain. However, well organized grain structures have been shown with additive manufacturing via control of process parameters such as the laser power, laser width, scanning path, scanning speed, etc. Based on the extensive experience in solving inverse problems in elasticity in general, the authors anticipate that a realistic and well organized grain structure will not pose more challenges than the artificial one using Voronoi Tesselation.

We notice that the quality of the reconstructions of the elasticity parameters in the first step (and consequently, the orientations in the following steps) decrease significantly with increasing noise levels. The error in the reconstructed angles from Table 10 is about 0% for the case of no noise. It ranges from 0% to 8% for the case of 0.1% noise and from 0% to 79% for the case of 1% noise. The error range in the reconstructions increases dramatically for 1% noise and needs further investigation. Thus, future work needs to

address the high errors in the reconstruction of some grains, in particular for noise levels of 1%. This could potentially be achieved by altering the regularization term or the norm to minimize the discrepancy between computed and measured displacement fields.

The average sub-domain sizes simulated in this paper are not representative of the actual grain sizes of zinc.<sup>34,35</sup> Using the realistic grain sizes would require a finer finite element mesh, extensive computations, and higher resolution for displacement acquisition if experiments are performed. Investigating the feasibility to translate this work on a finer mesh will be focus for future study. Also, we note that the inverse problem for the angle pair  $(\alpha, \beta)$  is not unique. A negation of the angle pairs,  $(-\alpha, -\beta)$ , will yield the same displacement field. Thus, future work will also focus on addressing uniqueness of the crystallographic orientation.

## Conclusions

In this article, we presented a novel approach to identify the grain-orientations for a class of anisotropic materials. Our identification method is based on the solution of inverse problems in linearized elasticity and full-field displacement measurements. We showcased the reconstructions of the grain-orientations obtained from the simulations for the cases with and without added noise. Further improvements in our algorithm and experimental validation could make our method potentially a viable tool to map the 3D crystal orientation of alloys.

## Acknowledgements

The authors would also like to thank the High Performance Research Computing at Texas A&M University for their computing resources.

## Author Note

Sevan Goenezen is now affiliated to Engineering Solutions and Quality Products, LLC, San Marcos, TX 78666, USA.


## Declaration of conflicting interests

The author(s) declared no potential conflicts of interest with respect to the research, authorship, and/or publication of this article.

## Funding

The author(s) disclosed receipt of the following financial support for the research, authorship, and/or publication of this article: The authors would like to acknowledge funding of this project from the National Science Foundation under Grant No. CMMI #1663435 and thank for their support.

## ORCID iD

Sevan Goenezen  <https://orcid.org/0000-0002-5051-4371>

## References

- Niendorf T, Leuders S, Riemer A, et al. Highly anisotropic steel processed by selective laser melting. *Metallurgical Mater Trans B* 2013; 44(4): 794–796.
- Hitzler L, Hirsch J, Heine B, et al. On the anisotropic mechanical properties of selective laser-melted stainless steel. *Materials (Basel)* 2017; 10(10): 1136.
- Hovig EW, Azar AS, Grytten F, et al. Determination of anisotropic mechanical properties for materials processed by laser powder bed fusion. *Adv Mater Sci Eng* 2018; 2018: 1–20.
- Vlassak JJ and Nix WD. Measuring the elastic properties of anisotropic materials by means of indentation experiments. *J Mech Phys Solids* 1994; 42(8): 1223–1245.
- Herrera-Solaz V, LLorca J, Dogan E, et al. An inverse optimization strategy to determine single crystal mechanical behavior from polycrystal tests: application to az31 mg alloy. *Int J Plast* 2014; 57: 1–15.
- Pant S, Laliberte J, Martinez M, et al. In-situ characterization of isotropic and transversely isotropic elastic properties using ultrasonic wave velocities. *Mater Perform Charact* 2016; 5(1): 164–188.
- Mei Y and Goenezen S. Quantifying the anisotropic linear elastic behavior of solids. *Int J Mech Sci* 2019; 163: 105131.
- Lekhnitskii SG, Fern P, Brandstatter JJ, et al. Theory of elasticity of an anisotropic elastic body. *Phys Today* 1964; 17(1): 84–84.
- Ting TCT. *Anisotropic elasticity: theory and applications*. Oxford: Oxford University Press, 1996.
- Miller VR and Miller RP. *René descartes: principles of philosophy*. Dordrecht, The Netherlands: Springer, 1984.
- Kobayashi K and Sugihara K. Crystal Voronoi diagram and its applications. *Future Gener Comput Syst* 2002; 18(5): 681–692.
- Sievers J. VoronoiLimit(varargin) – file exchange – MATLAB Central, <https://www.mathworks.com/matlab-central/fileexchange/34428-voronoilimit-varargin> (2021, accessed 17 August 2021).
- Tromans D. Elastic anisotropy of hcp metal crystals and polycrystals. *Int J Appl Sci Res Rev* 2011; 6(4): 462–483.
- Reddy JN. *An introduction to the finite element method*. New York, NY: McGraw-Hill, 2006. pp.27.
- Luo P, Mei Y, Kotecha M, et al. Characterization of the stiffness distribution in two and three dimensions using boundary deformations: a preliminary study. *MRS Commun* 2018; 8: 893–902.
- Barbone PE and Gokhale NH. Elastic modulus imaging: on the uniqueness and nonuniqueness of the elastography inverse problem in two dimensions. *Inverse Probl* 2004; 20(1): 283–296.
- Zhu C, Byrd RH, Lu P, et al. Algorithm 778: L-BFGS-B: Fortran subroutines for large-scale bound-constrained optimization. *ACM Trans. Math. Softw.* 1997; 23(4): 550–560.
- Oberai AA, Gokhale NH and Feij o GR. Solution of inverse problems in elasticity imaging using the adjoint method. *Inverse Probl* 2003; 19(2): 297–313.
- De Coninck A, De Baets B, Kourounis D, et al. Needles: toward large-scale genomic prediction with marker-by-environment interaction. *Genetics* 2016; 203(1): 543–555.
- Verbosio F, De Coninck A, Kourounis D, et al. Enhancing the scalability of selected inversion factorization algorithms in genomic prediction. *J Comput Sci* 2017; 22(Supplement C): 99–108.
- Kourounis D, Fuchs A and Schenk O. Toward the next generation of multiperiod optimal power flow solvers. *IEEE Trans Power Syst* 2018; 33: 4005–4014.
- Mei Y, Fulmer R, Raja V, et al. Estimating the non-homogeneous elastic modulus distribution from surface deformations. *Int J Solids Struct* 2016; 83: 73–80.
- Goenezen S, Kim BJ, Kotecha M, et al. Mechanics based tomography (mbt): validation using experimental data. *J Mech Phys Solids* 2021; 146.
- Carroll JD, Abuzaid W, Lambros J, et al. High resolution digital image correlation measurements of strain accumulation in fatigue crack growth. *Int J Fatigue* 2013; 57: 140–150.
- Di Gioacchino F and Quinta da Fonseca J. Plastic strain mapping with sub-micron resolution using digital image correlation. *Exp Mech* 2013; 53(5): 743–754.
- Pinto JMT, Touchard F, Castagnet S, et al. Dic strain measurements at the micro-scale in a semi-crystalline polymer. *Exp Mech* 2013; 53(8): 1311–1321.
- Walley JL, Wheeler R, Uchic MD, et al. In-situ mechanical testing for characterizing strain localization during deformation at elevated temperatures. *Exp Mech* 2012; 52(4): 405–416.
- Sutton MA, Li N, Joy DC, et al. Scanning electron microscopy for quantitative small and large deformation measurements part I: SEM imaging at magnifications from 200 to 10,000. *Exp Mech* 2007; 47(6): 775–787.
- Stinville JC, Echlin MP, Texier D, et al. Sub-grain scale digital image correlation by electron microscopy for polycrystalline materials during elastic and plastic deformation. *Exp Mech* 2016; 56(2): 197–216.
- Gianola DS and Eberl C. Micro- and nanoscale tensile testing of materials. *JOM* 2009; 61(3): 24–35.
- Du C, Hoefnagels JP, Bergers LIJC, et al. A uni-axial nano-displacement micro-tensile test of individual constituents from bulk material. *Exp Mech* 2017; 57(8): 1249–1263.
- Humphreys F. Review grain and subgrain characterisation by electron backscatter diffraction. *J Mater Sci* 2001; 36(16): 3833–3854.
- Humphreys FJ. Characterisation of fine-scale microstructures by electron backscatter diffraction (EBSD). *Scr Mater* 2004; 51(8): 771–776.
- Liu Z, Qiu D, Wang F, et al. Effect of grain refinement on tensile properties of cast zinc alloys. *Metallurgical Mater Trans A* 2016; 47(2): 830–841.
- Gokhale A, Sarvesha R, Prasad R, et al. A novel approach to refine surface grains in pure zinc using indentation scratch. *Mater Lett* 2019; 247: 151–154.